

Investigation of energy-relevant materials with synchrotron X-rays and neutrons

Ingo Manke¹, Henning Markötter¹, Christian Tötze^{1,2}, Nikolay Kardjilov¹, Roman Grothausmann¹, Martin Dawson^{1,3}, Christoph Hartnig⁴, Sylvio Haas¹, Diana Thomas¹, Armin Hoell¹, Christoph Genzel¹, John Banhart^{1,2}

¹Helmholtz Centre Berlin for Materials and Energy, Hahn-Meitner-Platz 1, 14109 Berlin, Germany

²Technische Universität Berlin, Materials Science and Technology, Hardenbergstr. 36, 10623 Berlin, Germany

³The School of Computing, Science & Engineering, University of Salford, M5 4WT, UK

⁴Chemetall GmbH, Trakehnerstr. 3, 60487 Frankfurt, Germany

Many materials used for energy conversion have a complex structure and chemical composition, knowledge of which is important for both understanding the function of materials and energy conversion systems and for their further development. Synchrotron radiation and neutrons can make an important contribution to understanding the function of such systems. Taking examples from the fields of fuel cells, gas separation membranes, batteries, solar cells and catalysts, the use of radiography, tomography, diffraction, scattering and absorption edge spectroscopy is demonstrated. The strength of such methods is the *in-situ* characterization of processes and compositions, and so the focus is on these aspects.

Keywords: Synchrotron X-ray, neutron, tomography, radiography, in-situ, diffraction, small-angle scattering

Author information

Dr. Ingo Manke, Head of Imaging Group

Henning Markötter, PhD Student

Dr. Christian Tötzke, Postdoctoral Fellow

Dr. Nikolay Kardjilov, Beamline Scientist Neutron Tomography

Roman Grothausmann, PhD Student

Dr. Martin Dawson, Physics Academic

Dr. Christoph Hartnig, Business Development

Sylvio Haas, PhD Student

Diana Thomas, PhD Student

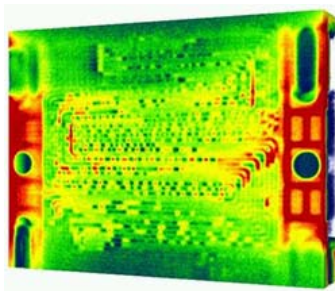
Dr. Armin Hoell, Beamline Scientist ASAXS

Dr. Christoph Genzel, Deputy Head of Institute of Applied Materials

Prof. Dr. John Banhart, Head of Institute of Applied Materials

Text and Graphic for Table of Contents

Fuel cells, gas separation membranes, batteries, solar cells and catalysts were investigated with synchrotron X-rays and neutrons to explore the process of synthesis, their internal structure and function. The aspect of in-situ characterisation is emphasised.



Neutron tomogram of a fuel cell stack.

1 Introduction

Materials or multi-material engineering components used in systems for energy generation or conversion can be very complex both chemically and with respect to their structure due to the multi-functionality required in many cases. This high level of complexity can also apply to the process of their synthesis or to the operation of the materials. Therefore, tools to gain insight into the synthesis, structure and operation of such materials – loosely called ‘energy-related’ in this article – are highly desirable. Both synchrotron X-rays and neutrons can be used for such investigations.^[1-3] The former because they are available as extremely intense monochromatic beams that allow both fast imaging, scattering or diffraction studies; the latter because of the unique interaction properties of neutrons with matter, of which the strong sensitivity to hydrogen and the weak interaction with most metals is the most prominent.

We present a collection of applications of both synchrotron X-rays and neutrons to the investigation of ‘energy-related’ materials. We use the generic methods radiography, tomography, small-angle scattering and diffraction in various combinations to demonstrate the power of these methods. The complementarity aspect, i.e. the fact that for example tomography can be carried out with X-rays and neutrons, is especially important. The systems investigated include fuel cells, catalysts used in such fuel cells, batteries and solar cells. The focus of the study varies: In fuel cells and batteries operation is studied, i.e. power generation; for catalysts the structure aspect is dominating; whereas for the solar cells the synthesis and grow process of the absorber layer is studied. Therefore, the criteria concerning temporal, spatial or q-space resolution are very different for these examples.

2 Experimental techniques and facilities

The fundamental interactions between neutrons and matter are very different to those between X-rays and matter, and produce very different beam attenuation properties.^[1,4] While X-rays interact with the charge distribution of the electron shell, the zero net charge of neutrons means that they mainly interact with the atomic nucleus. Therefore, the ability to use both sources, X-rays as well as neutrons, to characterize complex sample systems becomes more and more important in the framework of energy related materials.

We briefly review selected X-ray and neutron methods which have been used for the present paper. The associated beamlines are either located at the BESSY II storage ring or at the Hahn-Meitner-Reactor of the Helmholtz Centre Berlin.

X-ray beams produced at synchrotron facilities provide a very high brilliance, i.e. an intense, parallel beam over a wide X-ray energy range. This allows using either monochromatic or white radiation, with properties adjusted to the experimental tasks.

X-ray attenuation coefficients increase with atomic number (i.e. with the number of electrons), but the interaction probability of neutrons with the nucleus depends on the coherent scattering length, b_{coh} , which does not show a systematic dependence on atomic number. For the same reason, neutrons can penetrate macroscopic samples (up to tens of cm depending on the materials present) and distinguish between isotopes of the same element. Neutrons are highly sensitive to magnetic fields due to their intrinsic magnetic moment.^[5-11] The information yield by neutrons and X-rays is thus complementary as neutrons are relatively insensitive to most metals, but can be used to detect small amounts of many light elements, including hydrogen, boron and lithium. These properties make neutrons ideal for applications in a wide range of scientific and industrial applications.^[1-2,4,12-21] Most neutron imaging facilities use either cold or thermal neutrons ($\sim 2-25$ meV) since at these energies neutrons have relatively large effective interaction cross-sections with matter, but are still able to penetrate bulk matter (c.f. energies of 10-100 keV used for similar experiments with X-rays). Neutron experiments require high intensity in a beam that is well-defined (collimated) and must therefore be conducted at large experimental facilities such as nuclear reactors or spallation sources.

2.1 X-ray tomography

Synchrotron X-ray imaging experiments were performed at the BAMLine facility at BESSY (HZB, Germany).^[22] A W-Si multilayer monochromator with an energy resolution of about $\Delta E/E = 10^{-2}$ was used to obtain a monochromatic X-ray beam, and energies between 10-20 keV were selected to provide both good transmittance through the fuel cell components and sufficient sensitivity to liquid water. A CCD camera (2048×2048 pixel Princeton VersArray 2048B) was used to capture images up to 16×10 mm² in size with image pixel sizes between 0.3 and 4 μm . Typical measurement times per image were between 1 and 5 s.

2.2 White X-ray diffraction

The materials science beamline EDDI (*Energy Dispersive Diffraction*) is operated in the energy dispersive mode of diffraction using a high energy white photon beam with an energy range from 15 to 150 keV.^[23] In contrast to angle-dispersive diffraction, energy dispersive X-ray diffraction (EDXRD) yields complete diffraction patterns, which are recorded under a

fixed scattering angle 2θ . EDXRD is a powerful tool to investigate problems in different fields of materials science. Due to the wide energy range of the synchrotron radiation and a good time resolution it is possible to analyze structural properties and gradients in the near surface region of polycrystalline materials. Residual stress- or composition gradients, but also texture and microstructure of different materials can be analyzed. Moreover *in-situ* experiments at ‘room’ and high temperature, for example the growth of chalcopyrite $\text{Cu}(\text{In,Ga})(\text{Se,S})_2$ thin films, can be explored.

2.3 Anomalous small-angle X-ray scattering (ASAXS) and small-angle neutron scattering (SANS)

Anomalous small-angle X-ray scattering is a versatile tool for the non-destructive determination of structural parameters in combination with element sensitivity and is used to study materials containing nm-sized compositional fluctuations.^[24-25] ASAXS experiments were performed at the 7T-MPW-SAXS beamline at the storage ring BESSY II.^[26] Figure 13 illustrates the basic experimental setup.

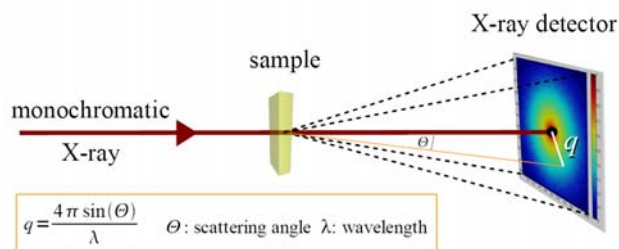


Fig. 1. The figure shows a sketch of the experimental setup to perform small angle X-ray scattering. In case of anomalous small angle X-ray scattering (ASAXS), the X-ray energy is tuned in the vicinity of X-ray absorption edges of the elements present in the sample. This will cause a change in the differential scattering cross section, which can be analysed.

The X-ray energy was selected in the range 4 - 27 keV by a Si (111) double-crystal monochromator with an energy resolution of $\Delta E/E \sim 10^{-4}$. The small-angle scattering patterns were recorded at several selected X-ray energies in the vicinity of X-ray absorption edges of the elements of interest. A 2D multi-wire proportional counter (1024×1024 pixels; pixel size $\sim 200 \mu\text{m}$) was used to measure the intensity scattered by the sample. Standards such as glassy carbon or silver behenate were measured in addition to calibrate the relative intensities to differential scattering cross sections as function of the absolute value of the scattering vector q . The energy dependency of these cross sections yields information about the spatial arrangement of the resonant element after appropriate analysis.

Complementary to ASAXS, small-angle neutron scattering (SANS) experiments were carried out at the beamline V4 of the Hahn-Meitner-Reactor of the Helmholtz Centre Berlin.^[27] The basic principles of SANS and SAXS are the same, the difference being the interaction of the beam with the sample and therefore the resulting scattering contrast. A unique option for contrast enhancement is to exchange isotopes of a given element, since neutron scattering can vary strongly for different isotopes of a given element. An example is the exchange of H₂O by D₂O or even by a mixture of both kinds of water.

2.4 Neutron radiography and tomography

Neutrons were first used to create images in 1935 by Kallmann and Kuhn in Germany, but development of the techniques was stymied by the complexity of the experimental set-up and the extremely long exposure times involved (several hours were required for a single radiographic image).^[1,28] Currently, neutron radiography and tomography and other associated techniques are experiencing rapid advancement.

The neutron imaging measurements shown in this paper were performed at the CONRAD (V7) facility (HZB, Germany).^[29] CONRAD is located in the neutron guide hall of the Hahn-Meitner research reactor BER-II at the end of a curved neutron guide, which delivers an almost pure cold neutron spectrum – peak wavelength ~ 3.1 Å – with a negligible component of thermal and epithermal neutrons and γ rays. The detector system consists of a 16 bit low-noise Andor DW436N-BV CCD camera (2048 \times 2048 pixel²), which is focused by a lens system on a neutron-sensitive scintillator screen. In order to prevent radiation damage of the camera the image from the scintillator is reflected by 90° by a mirror. The sample environment is equipped with translation tables, which allow the sample to be manipulated remotely into any position in or around the beam.

Radiography is based on the position-sensitive detection of intensity variations across a radiation beam in the 2D plane perpendicular to the direction of beam propagation. This beam attenuation is indicative of structural features of samples placed within the beam such as varying material thickness, the presence of cracks or voids and chemical composition. By measuring multiple projection images as the sample is rotated around an axis parallel to the detection plane it is possible to reconstruct the 3D volumetric attenuation properties of a sample, revealing features that are often not clear in single projections; these 3D methods are called tomography^[1].

The standard data processing involves using the dark current signal (an image where no external radiation impinges upon the detector) and the open beam signal (an image of the

beam profile in the absence of a sample) and to normalize data images. This removes detector and beam inhomogeneities. However, in some cases it is more appropriate to use the initial condition of the system rather than the open beam as the reference image such that only those parts of the experiment that changed in the course of an experiment are revealed (referred to as quotient images). This is particularly important in extracting quantitative information from experiments where changes are difficult to detect, e.g. in fuel cells, where the beam attenuation caused by the water distribution is much smaller than the attenuation caused by the structure of the cell.

2.5 Electron tomography

Electron tomography is a complementary method to ASAXS to determine the structure and sizes of particles of catalytic materials. The three-dimensional representation of the sample allows for more detailed and exact evaluations, but only on very small volumes of about (500 nm)³. Electron tomography is also a more difficult and more time consuming method than ASAXS considering the evaluation of size distributions.

The reconstruction of the three-dimensional representation of the sample is based on a series of projection images taken at different orientations of the sample in the Transmission Electron Microscope (TEM).^[30] In most cases, the sample is tilted step by step around a fixed rotation axis. At each step an images is acquired. In this way, all images form a tilt series. In most cases it is not possible to acquire images in the TEM over a full range of 180° because of sample intransparency or space limitations in the specimen chamber.

Electron tomography needs a very careful sample preparation because the samples have to be thin enough (below 500 nm) to be electron-transparent over the entire tilt range of $\pm 75^\circ$. Additionally, fiducial markers (mostly gold nanoparticles with 2–15 nm diameter depending on magnification) can be added to the sample for the later fine alignment of the tilt series images.

At typical magnifications used in electron tomography ($> 10000\times$) the mechanical instability of the goniometer cannot be neglected any more. Therefore features in the sample have to be tracked during acquisition of the tilt series. A software controlling the TEM automatically re-centres and re-focuses the sample features after each tilt increment during the acquisition. After acquisition of a tilt series the images have to be aligned to each other. A coarse alignment of successive images by cross correlation is mostly followed by a fine alignment. This is achieved by a software (e. g. IMOD^[31]) that calculates even local distortions with

manually tracked markers. Finally, the tomogram of the sample detail can be reconstructed from the aligned images of the tilt series. There are different reconstruction algorithms available, e.g. WBP (Weighted Back Projection), SIRT (Simultaneous Iterative Reconstruction Technique), ART (Algebraic Reconstruction Technique), DART (Discrete Algebraic Reconstruction Technique)^[32] and DIRECTT (Direct Iterative Reconstruction of Computed Tomography Trajectories).^[33-34] Filtering the reconstructed tomogram can reduce noise and reconstruction artefacts. After this, a binarization for each identified material or region is necessary for further analysis of e.g. volume or surface area.

3 Fuel Cells

Low temperature polymer electrolyte membrane (PEM) fuel cells are currently the most important fuel cell type in respect to their function as possible future alternative energy sources, particularly in mobile applications.^[35-40] In commercial applications, a PEM fuel cell has to adapt to huge variations in environmental and operating conditions, especially current load. A typical PEM fuel cell (Fig. 1) consists of several components: the PEM membrane (usually Nafion) in the centre surrounded on both sides (anode and cathode) by the catalyst, the gas diffusion layer (GDL), the flow field channels and the end plates.

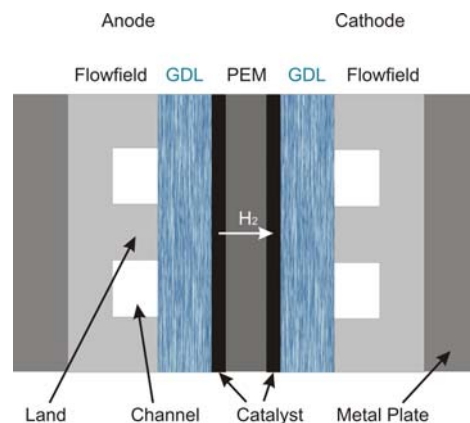


Fig. 2. Diagram of the cross-section of a typical PEM fuel cell.

Liquid water plays a crucial role in these fuel cells and strongly affects the power output of the cell and the longevity of the materials and components used. The membrane used in PEM fuel cells is typically made of Nafion, which is only proton conductive when wet. The proton conductivity of the membrane is improved with increasing humidity. A reduction of the membrane humidity results in significant power losses and even severe damage.^[41-42] The

wetness of the membrane must therefore be maintained under any operating condition. However, liquid water is a major cause of flooding in the porous gas diffusion layer (GDL) materials and flow field channels, which is known to lead to significant power loss in operating fuel cells and could even lead to a complete breakdown of the output power.^[36,40,43-44] For these reasons, water management is one of the key issues in the development of high-power, long-life hydrogen PEM fuel cells.^[45-46]

In order to understand water management issues, it is essential to study the liquid water distribution, the water transport mechanisms and the influence of different materials on transport behaviour. Numerous theoretical and experimental reports focusing on two-phase flow have provided a crucial insight into the basics of water transport^[47-65], but direct observation of the water flow dynamics in an operating cell is central to understand the underlying phenomena.

In recent years, neutron radiography^[66-80], magnetic resonance imaging^[81-82] and X-ray imaging^[83-89] have been successfully applied to visualize liquid water flow in fuel cells. Magnetic resonance imaging is only suited for very small cells, which must be made of non-metallic materials and contain catalysts with a reduced Pt-load in order to prevent strong image artefacts. Synchrotron X-rays and neutrons are, therefore, more practical for the investigation of liquid water in operating fuel cells.

The first use of neutron radiography for such studies was reported in 1999^[66] and improvements to the technique over the following years have allowed tomographic studies of entire PEMFCs, allowing cell-by-cell detection of liquid water agglomerates. The combination of imaging measurements with locally resolved current density or impedance measurements reveals the correlation between water distribution (agglomeration/dehydration) and the local efficiency/activity of the respective area in the cell. This was demonstrated experimentally at the Hahn-Meitner-Institute (now HZB) in 2007 using synchrotron X-rays for *in-situ* measurements of small water agglomerations in the gas diffusion layers.^[83] Such experiments are currently not possible with neutron techniques due to the high spatial resolution required.

3.1 In-situ synchrotron radiography of water and CO₂

3.1.1 In-plane view (parallel to the active layer)

For the X-ray investigations, a cell was designed and fabricated by the Centre for Solar Energy and Hydrogen Research, Ulm (ZSW).^[84] The cell had one meander flow field channel

machined in carbon composite plates, and had a narrow section containing a single vertically oriented channel to allow better transmission of X-rays (Fig. 2). In this region, the observed catalytic active area was supplied by one channel on each side surrounded by land sections.

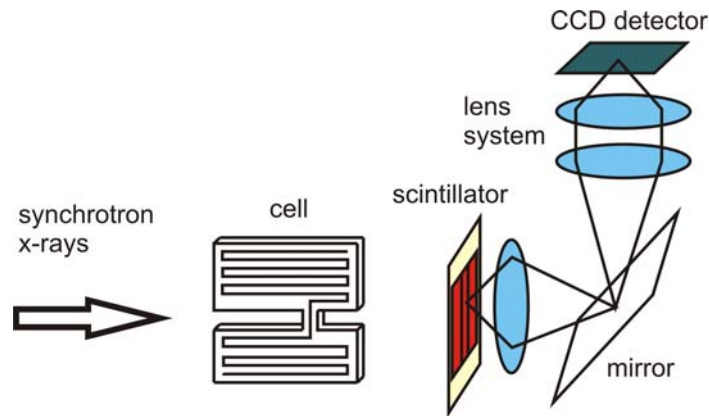


Fig. 3. In-plane view: the PEM fuel cell designed to allow high resolution radiographic imaging of a single flow channel.

3.1.2 Low temperature PEM fuel cell (LT-PEM)

Figure 3 shows six images of the start-up process of a LT-PEM. Water (white) is produced at the cathode side of the membrane during catalytic reaction, see Table 1.^[37]

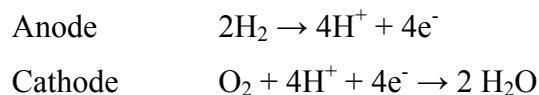


Table 1. The catalytic reaction that produces liquid water at the cathode.

Using an empty cell as the reference, the water distribution can be mapped. The bright areas in Fig. 3 correspond to water agglomerations that arise first at the cathode side of the cell in the gas diffusion layer (GDL), which fills up with water preferentially next to the hydrophobic microporous layer (MPL) and at the flow field beneath the land sections (Fig. 3 c and d).^[84] Water migrates through the GDL into the channel, where it is either carried away by the convective gas flow or evaporates. Below the land sections of the flow field the convective influence is much lower and water agglomerations arise in the pores of the GDL as seen in Fig. 3 b and c. Due to diffusion processes through the membrane, water also occurs at the anode side and fills up the GDL in a similar way there (Fig. 3 e and f).

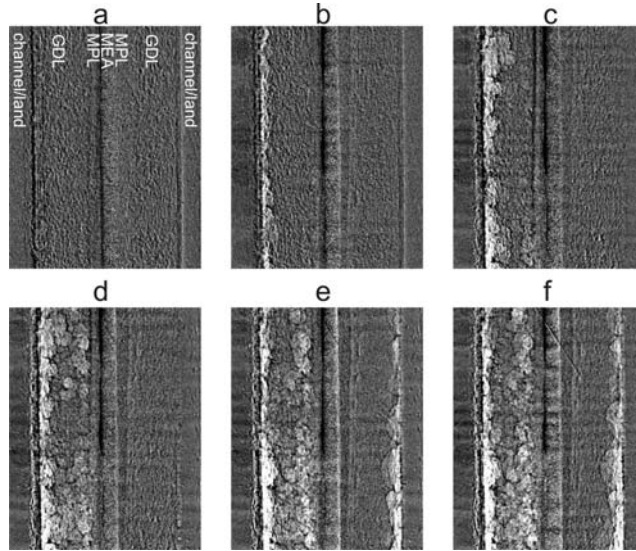


Fig. 4. Radiographic quotient images of the start-up process of a low temperature PEM fuel cell (cathode left, anode right).^[84]

During this sequence, a slight displacement of the membrane electrolyte assembly (MEA) can be detected, that is caused (among other factors) by an increasing water content of the membrane. The membrane is initially not fully humidified with water (this only occurs during cell operation) but later increased humidification of the membrane changes its structure and causes it to expand. Full proton conductivity is given when the membrane is sufficiently wet, so a complete drying of the membrane should be avoided..

3.1.3 Direct methanol - PEM fuel cell (DMFC)

For the test DMFC, a MEA (membrane electrolyte assembly) based on a Nafion 115 combined with a carbon cloth GDL (Fig. 4 b) was grouted at the ZSW. A platinum catalyst (2.5 mg/cm²) was used at the cathode and a platinum/ruthenium catalyst (2.0 mg/cm²) at the anode. The geometry of the cell investigated was similar to that shown in Fig. 2. This type of fuel cell operates using a water methanol mixture at the anode and air at the cathode. The catalytic reaction produces CO₂ at the anode and water at the cathode, see Table 2.

Anode	$\text{CH}_3\text{OH} + \text{H}_2\text{O} \rightarrow 6\text{H}^+ + 6\text{e}^- + \text{CO}_2$
Cathode	$1 \frac{1}{2} \text{O}_2 + 6\text{H}^+ + 6\text{e}^- \rightarrow 3 \text{H}_2\text{O}$

Table 2. Catalytic reaction producing water at the cathode and CO₂ at the anode.

After processing the images of the operating fuel cell, CO₂ bubbles became visible at anode side.^[86] Figure 4 illustrates a further property of quotient images in that any CO₂

agglomerations in the initial conditions of the experiment are inverted in the quotient image, appearing as bright regions (Fig. 4, white arrow). In DMFCs it is difficult to achieve a bubble-free state at the anode and a water free state at the cathode simultaneously, as the fuel (methanol) is usually supplied as aqueous solution and electrochemical side reactions cannot be completely excluded. The carbon fibre bunches of the GDL act as gas flow barriers, so CO₂ agglomerations occur primarily below them. Some CO₂ bubbles move to the end of the fibres and into the channel and are identifiable in the images (Fig. 4 a, black arrow). Once the bubbles are dragged by the fluid flow along the channel, they cannot be resolved temporally, resulting in an almost homogeneous darkening of the channel. By tracking these CO₂ bubbles it can be seen that they follow the path of least resistance between the carbon fibre bunches. A tomography of a carbon cloth GDL (Fig. 4 b) shows the structure of the material. In 500 μm intervals the fibre bunches change their orientation, forming gaps that act as the primary transport routes of the CO₂.

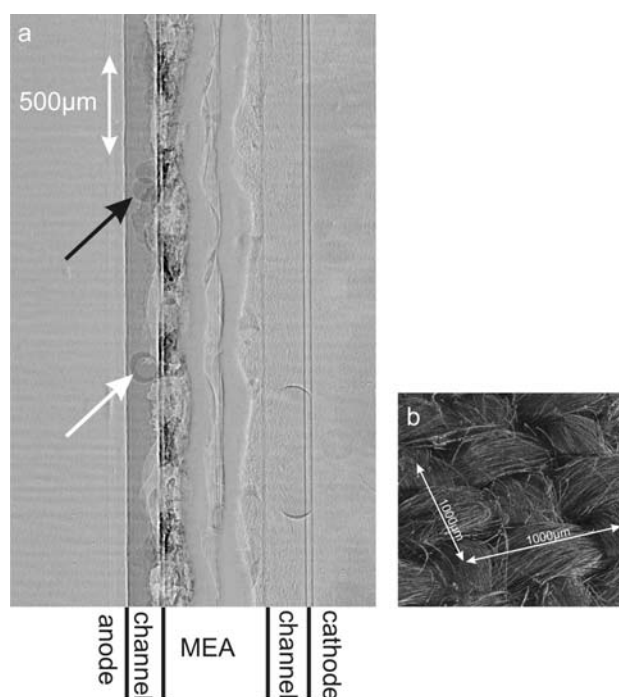


Fig. 5. (a) In-plane radiography of a direct methanol fuel cell, showing CO₂ that has moved after the start of the experiment (white arrow) and newly formed CO₂ bubbles moving into the GDL (black arrow). (b) A tomography of a carbon cloth GDL structure shows the structure of the GDL fibre bunches.^[86]

3.1.4 Through-plane view (perpendicular to the active layer)

In order to image the layer perpendicular to the active one, it would be necessary for the X-ray beam to transmit the MEA (membrane electrode assembly), the GDL, the current collector plates and the massive endplates. In order to allow beam transmission the current collector plates and the endplates were speared (Fig. 5).

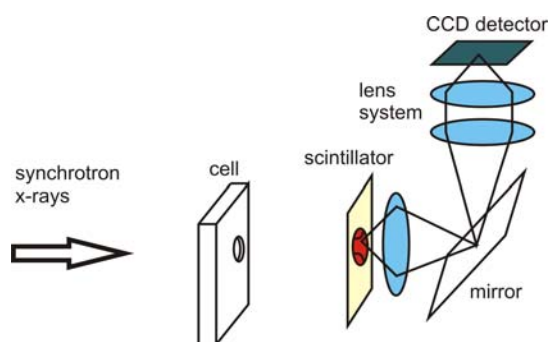


Fig. 6. Through-plane view: the massive endplates and the metallic current collector plates of the cell are speared in a small area.

Figure 6 shows the point at which the flow field channels turn at the border of the cell. CO₂ permanently follows the channels to the exit tubes, which is why they appear dark in the picture. In this through-plane view, the presence of CO₂ agglomerations in the GDL is clearly visible. The dark areas periodically arranged every 500 μm in Fig. 6 reveal the correlation between GDL structure and CO₂ transport. From this view it is also possible to study water formation processes, though this is complicated by the superposition of the anode and cathode. Small cracks can also be seen in the catalyst (white arrow in Fig. 6), which are filled with CO₂ and are expected to play a role in CO₂ transport. These cracks originate from the manufacture of the MEA where the catalyst layer is sprayed onto the membrane. Upon drying the catalyst layer shrinks and cracks occur. It is thus clear that manufacturing characteristics also play a role in the CO₂ transport.

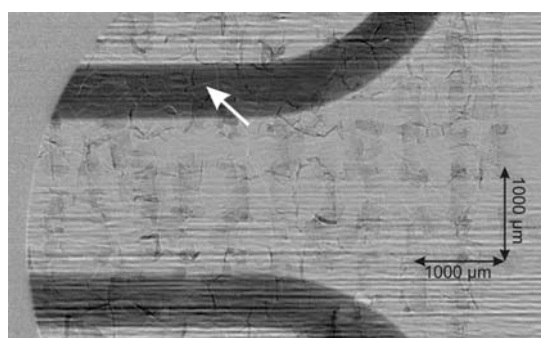


Fig. 7. Through-plane radiography reveals the structure of the GDL.^[85]

3.2 *In-situ neutron radiography*

The ability of neutrons to penetrate thick metallic components while being very sensitive to small amounts of hydrogen make them ideal for investigating the water distribution in an entire fuel cell without any need for modification and therefore artificial changes of the observations. Furthermore, the whole active area of a fuel cell with typical widths of a few to

20 cm can be imaged, providing a picture of transport processes within the cell, including the inlets and the outlets. Figure 7 a shows a neutron radiograph of a PEM fuel cell with a total size of $14 \times 14 \text{ cm}^2$. In the inner part, some dark areas (i.e. high attenuation) can be seen that can be assigned to local water accumulations in the flow field channels. This is a good example of where quotient imaging greatly improves the ability to quantify the water distribution inside the cell (water distribution shown in Fig. 7 b).

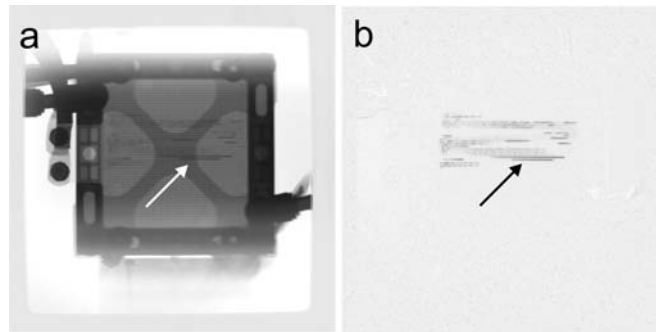


Fig. 8. Neutron radiographs of an operating PEM fuel cell. a) the dark horizontal lines are caused by the strong attenuation of water in flow field channels. b) two-dimensional liquid water distribution after normalisation.^[90]

A very promising new technique is the combination of neutron radiography with current density mapping. For this purpose, a special board with shunt resistors embedded in a segmented multi-layer printed circuit board with a segment size of $2 \times 2 \text{ cm}^2$ was integrated into the fuel cell.^[91]

From the characteristic locally resolved current measurements it is possible to correlate the water content and/or starvation effects due to insufficient gas supply with the performance of the cell. This is illustrated in Fig. 8. The local current density is reduced in the lower and the upper sections of the cell and the reasons why can be found from a radiograph of the water distribution. In the lower part of the cell the flow field channels are filled with water (dark horizontal lines), greatly reducing the gas supply of the catalyst. In the upper part of the cell (especially on the right side) very little water can be seen and the humidification is too low for the cell to operate efficiently.

This combined approach allows detailed studies on the effects of GDL properties such as investigations of the influence of the anode and cathode GDL wettability on the current and media distribution in a DMFC. Different MEAs were prepared by vertically splitting either the anode or cathode carbon cloth GDL into a less hydrophobic part (untreated carbon cloth) and a more hydrophobic part (carbon cloth impregnated by PTFE dispersion).

As mentioned above not only the water, but also the CO₂ distribution is of interest in a DMFC. These two can usually be separated in images after the normalization procedure. CO₂ bubbles in the methanol-water mixture increase the local transmission (i.e. make the region brighter), while water droplets decrease the transmission signal (i.e. make the region darker) as in Fig. 9 a.

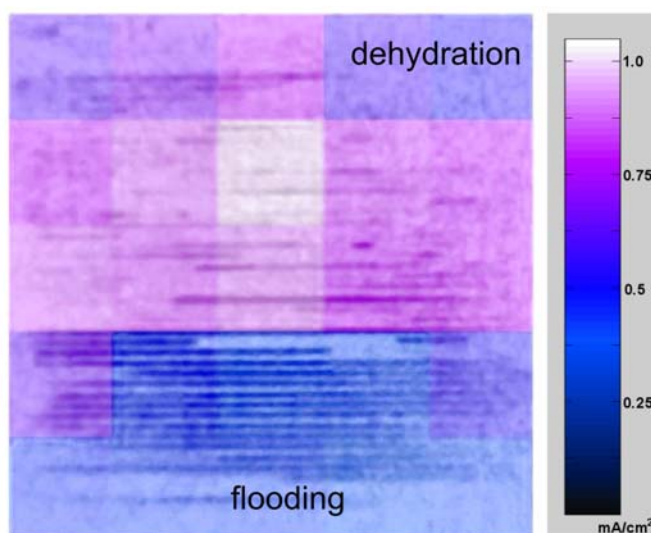


Fig. 9. Colour map of the current density measurement overlapping the corresponding normalized neutron radiograph, showing the correlation between the water distribution and the electric current density in a PEM fuel cell. The dark horizontal lines can be assigned to liquid water in the flow field channels (compare to Fig. 7). The measurement reveals that low performance of the cell is related to a simultaneous flooding of the lower part of the cell and dehydration of the upper right part.^[74]

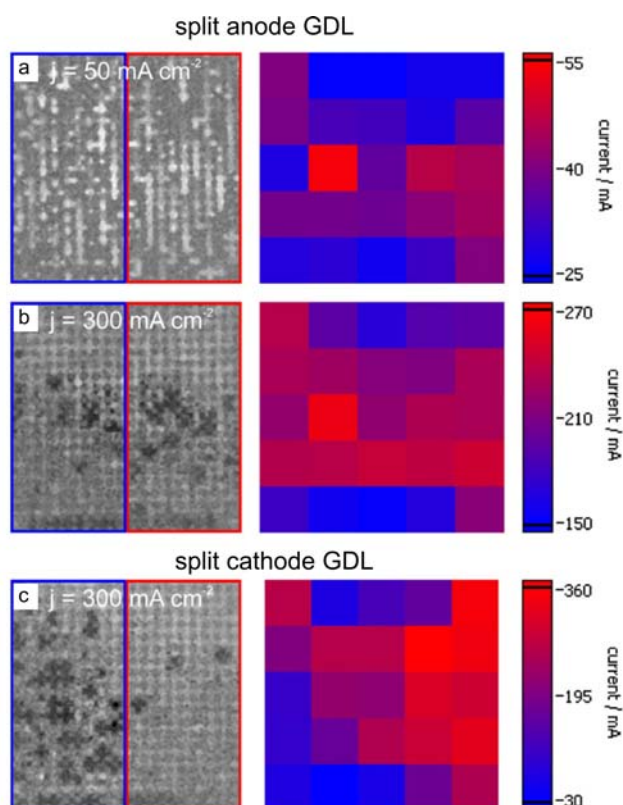


Fig. 10. Normalized radiographs (left side) and the corresponding current distributions (right side) of a MEA with a vertically split carbon cloth gas diffusion layer a) and b) on the anode side and c) on the cathode side (Reprinted with permission from Elsevier).^[78]

At low current densities mainly CO₂ (located at the anode) and only limited amounts of water (at the cathode) can be seen (Fig. 9 a). When the current density is increased to 300 mA/cm² several dark spots appear indicating liquid water produced at the cathode.

In Figs. 9 a and b, showing a DMFC with a split anode GDL, hardly any effect of the GDL hydrophobicity can be observed. CO₂, water and current density are similar on both the left and right side of the cell. When the cathode GDL is split instead, the current density on the side with the hydrophilic GDL (left side in Fig. 9 c) is strongly reduced. The reason can clearly be seen: flooding on the left side due to excessive liquid water production. On the hydrophobic side the water is still balanced and the current density is about 60% higher than that of the hydrophilic side.

3.3 *Synchrotron X-ray tomography supported materials modelling*

Because of the high available flux and the monochromatic X-rays of the synchrotron used, tomography provides high quality images that allow the investigation of interesting structure details as well as small variations in material composition.^[1-2,92-97] In fuel cell research structural investigations of the GDL materials are very useful for visualizing the structural aging of the used materials.

Modelling and fluid transport and distribution simulations are an important part of GDL design as they allow material parameters to be altered and tested without the expense or time-consuming manufacture. However, to produce realistic results these simulations need realistic input data, which synchrotron X-ray tomography can supply through high-resolution 3D studies of GDL structures. An example is shown in Fig. 10, where the carbon fibres and the binder between the GDLs are both visible. Real structural parameters such as pore size distribution, tortuosity and connectivity, which are closely related to the media transport properties of the GDL, have been analyzed and a mathematical algorithm to create GDL models with similar properties was developed (by Thiedmann et al.).^[94-95] Figure 11 shows the fibres (bright) which were created by this model. The black lines are possible paths through the materials that can be taken by a gas or water stream. One of the main characteristics of GDL materials is their tortuosity, i.e. the length of the direct connection between catalyst and channel compared to the paths through the materials; obviously the paths through the GDL are longer. The tortuosity distributions for all possible paths are given in

Figs. 12 a and b for the real material and the model, respectively. They are in agreement and the model is shown to be a good representation of the real system.

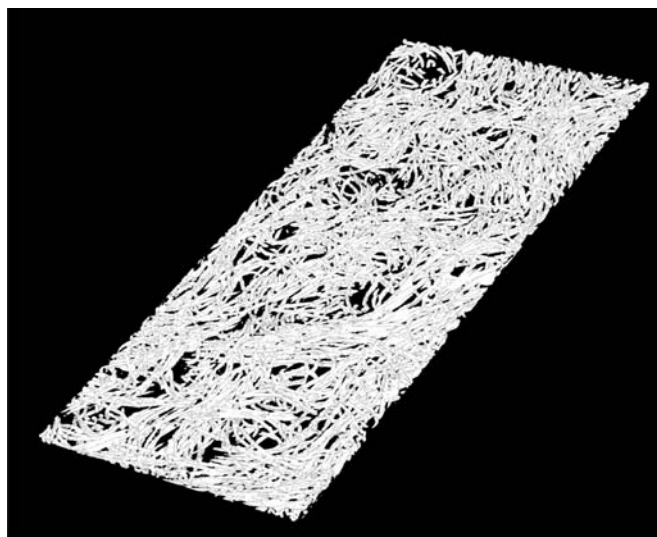


Fig. 11. Part of a synchrotron X-ray tomograph of a gas diffusion layer, displaying the carbon fibre distribution (white).

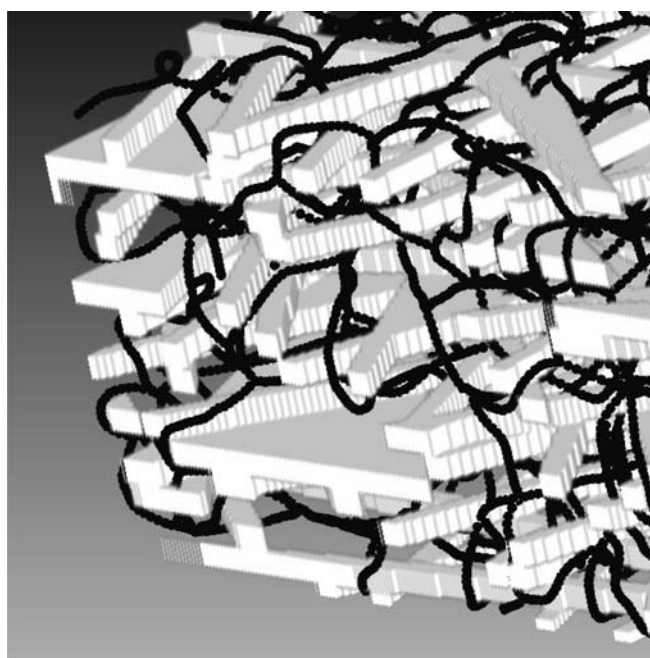


Fig. 12. Calculated paths through the pore space of a modelled GDL (white = fibres). (Reproduced by permission of The Electrochemical Society).^[94]

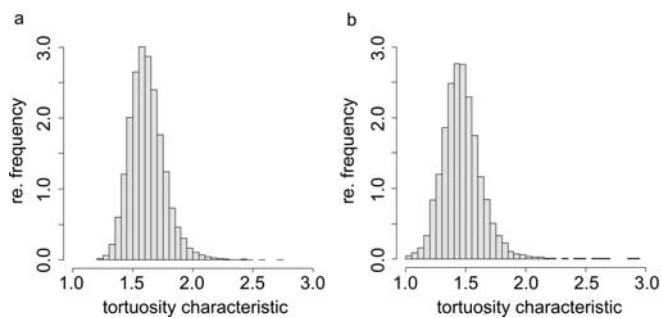


Fig. 13. Comparison of the tortuosity characteristic of the model (a) and a data set of a real GDL (b) obtained by synchrotron X-ray tomography (Reproduced by permission of The Electrochemical Society.)^[94]

4 Catalysts

4.1 Anomalous small angle X-ray scattering (ASAXS)

To meet future energy demands there is an urgent need for higher and better performing heterogeneous catalysts for fuel cell applications, characterised by reduced amounts of noble metals. A promising development is the replacement of Pt by less expensive metals. In a recent study, selenium-modified ruthenium nanoparticles supported by activated carbon (Black Pearls 2000 from Cabot) have been found to catalyse the oxygen reduction reaction (ORR) in acidic media with high activity and superior selectivity.^[98] Therefore, this system is now in the focus of attention as methanol-tolerant electrocatalyst meant to replace Pt at the cathode side of Direct Methanol Fuel Cells (DMFC).^[99-101] For future development and to pave the way towards commercial applications, a better understanding of this novel catalyst system is indispensable. Highly active RuSe_x/C catalysts were prepared in a multistep procedure starting from ionic metal precursors,^[102] which is in contrast to traditional preparation techniques.^[103] The optimum Se content was found to be at about 7 wt.% on a sample containing about 40 wt.% Ru and gave the highest electrochemical activity.^[104]

ASAXS has recently been demonstrated to provide useful information about chemical compositions on the nanometer scale.^[105-106] As heterogeneous precious metal catalysts mostly consist of the nm-sized metal particles supported on chemically inert carriers,^[107-108] ASAXS is an ideal tool for their characterisation. To deduce an applicable structural model of the nanoparticles in the aforementioned system, a RuSe_x catalyst with 40 wt.% Ru and 14 wt.% Se reduction-annealed at 800°C was characterized in detail by ASAXS. The contrast variation (ASAXS) was performed at five different energies near but below the Ru-K absorption edge at E=22117eV.^[109-110] In this case, the anomalous scattering effect of the Ru atoms is utilized, which allows for the calculation of the resonant, mixed-resonant and non-

resonant partial scattering contributions using the method introduced by Stuhrmann.^[111] The resonant contribution contains information about the spatial arrangement of the resonant scattering element alone, here the Ru atoms. The non-resonant contribution describes the behaviour one would get from measurements at X-ray energies far from the absorption edges of the elements present in the sample. Therefore, this term contains information about all structure components and elements of the sample. The third term is the mixed-resonant and represents a cross term.

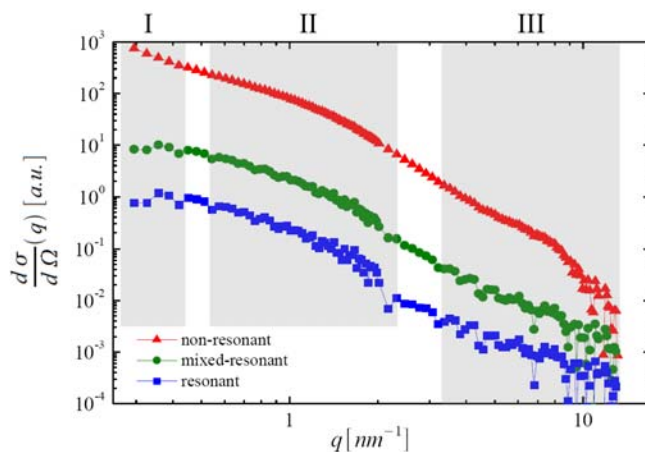


Fig. 14. Three energy-independent scattering fractions (non-resonant, mixed-resonant and resonant) of the catalyst sample RuSe_x/C , which have been obtained by a dispersion analysis of ASAXS at the Ru edge.

In Fig. 14 the obtained energy-independent partial scattering contributions as function of the absolute value of the scattering vector q of the RuSe_x/C catalyst are shown in a log-log representation. The main result of this analysis was that the scattering curves can be split into three regions (I, II and III). In the limit to small q -values (region I) the resonant scattering curve converges to a constant intensity value contrary to the non-resonant curve, which shows a strong increase towards smaller q -values. This indicates the presence of a large structure element not containing Ru, namely the carbon support. In the limit of large q -values (region III) the resonant curve shows a linear decrease in this representation, contrary to the non-resonant curve, which shows a weak broad peak in this q -domain. Therefore, the scattering caused by the nanostructure has almost nothing to do with Ru in the sample, since in this case the underlying nanostructure should also be detectable in the resonant scattering contribution that represents the spatial arrangement of the Ru atoms. Region II, finally, comprised the small-angle scattering of one species of nanoparticle, which has to be considered as Ru particles.

Dispersion analysis shows that a structural model with three independent particle species (in size and composition) has to be adopted to describe the structure of the catalyst correctly.

Figure 15 shows the volume-weighted size distributions of all three components and a sketch of the suggested structural model.^[109-110] The three species are assumed to be connected with the following structures: (i) the carbon support (Black Pearls) with a mean radius of 15.00 ± 5.70 nm; (ii) Ru particles with a mean radius of about 1.25 ± 0.60 nm; (iii) Se aggregates with a mean radius of about 0.30 ± 0.02 nm.

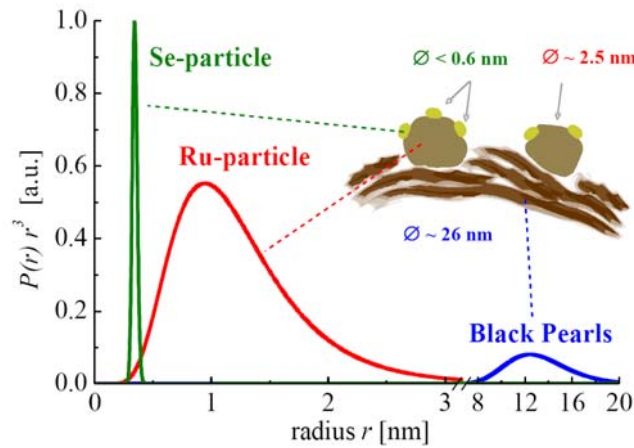


Fig. 15. Suggested structural model derived from ASAXS and afterwards affirmed by SANS.

In a further step, the complementary technique of small-angle neutron scattering (SANS) was applied to confirm the structure model derived by ASAXS. To describe the SANS curves the scattering contrast for each contribution and the general scattering background have to be assumed separately. In Fig. 16, a comparison between SAXS and SANS curves of the active catalyst sample RuSe_x/C is shown. Additionally, the fitted structural model curves for both cases are illustrated. Obviously, both the SAXS and SANS curves are well described by the theoretical model within the error band/bar of the measured values.

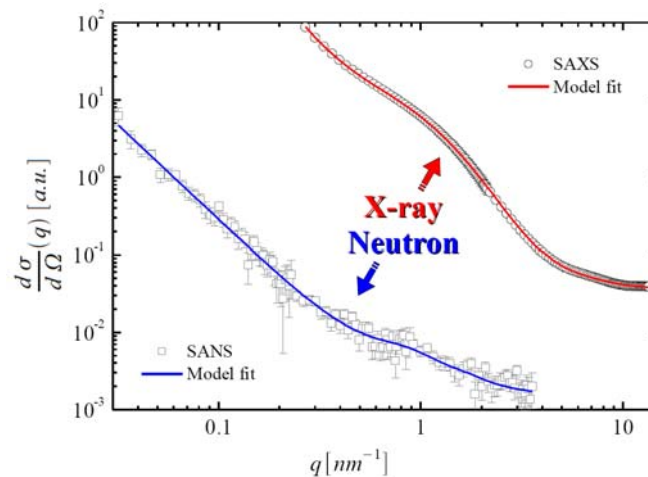


Fig. 16. *Small-angle scattering curves of the active catalyst sample RuSe_x/C measured using X-ray (SAXS) and neutron (SANS) as complementary methods. Both curves can be described by the same structural model by exchanging the scattering contrast and background contributions, respectively.*

The proposed structural model is not only supported by previous results of conventional characterisation techniques (e.g. XRD, TEM and EXAFS).^[104] In fact, recent improvements of the experimental setups for ASAXS and numerical calculations revealed for the first time that Se-modified Ru nanoparticles on RuSe_x/C catalysts are not completely covered by Se as previously proposed. Se rather forms small patches on the Ru surface, while the rest of the surface is covered most likely by oxygen. The complementary use of X-ray and neutron radiation for this analysis confirms the derived structure model from ASAXS alone. In the example presented SANS was not necessary to deduce the model from ASAXS, but for other complex sample systems the complementary use of both sources can be essential to achieve a comprehensive view of the nanostructure.

In further studies of heterogeneous catalysts ASAXS will be used to monitor the *in-situ* structural changes of the active nanoparticles during the ORR process. This will allow for a deeper insight into the process of ORR. ASAXS could also be used to characterize a wider range of nanostructured materials in the framework of renewable energies (e.g. thin films solar cells, quantum dots on surfaces for third generation solar cells) or in the framework of energy storage (e.g. battery, hydrogen storage materials) or in the framework of energy conversation (e.g. catalyst materials for fuel cells).

4.2 *Electron tomography*

Since catalysis takes place at the surface of a catalyst the aim is to create a catalyst material that needs as little ruthenium as possible (to save costs) but that has much catalytic surface. It is therefore not only important to know the size distribution of the ruthenium particles^[104] but also the position of the ruthenium particles in relation to their carbon support to improve the catalytic effectiveness. A typical TEM image of such a material is shown in Fig. 17. The large grey areas are assigned to the carbon support particles and the small dark location on the surfaces to the Ru catalysts.

Depending on the preparation of the catalytic material the ruthenium particles are mostly on the surface of the support particle or inside. If they are on the carbon support surface they have more “free” surface (meaning that the surface that is not covered by carbon) for catalysis than if they are inside. This information is hardly obtained by single TEM images. Electron tomography provides much deeper insights into the distribution of the Ru particles relative to

the carbon support. The reconstructed tomogram in Fig. 18 shows the Ru particles on the carbon surface. The particles are partly embedded into the carbon, an information that is of importance for the understanding of their catalytic activity and the suitability of different preparation processes.

This demonstrates that electron tomography is not only a complementary method to SAXS but also yields valuable additional information about texture, structure, morphology and configuration of the ruthenium based catalysts.

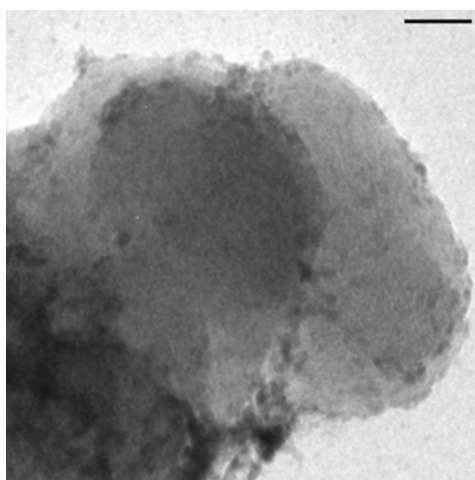


Fig. 17. A ZL-TEM image (Zero-Loss: Only elastically scattered electrons contribute to the image) of ruthenium based catalyst material. The image shows the big carbon support particle and on its surface (possibly also inside) the ruthenium particles (darker, about 5 nm big). The carbon particle sticks to a carbon foil (light grey background) with gold markers (dark spots on the foil around 1 nm big). The scale bar is 20 nm wide.

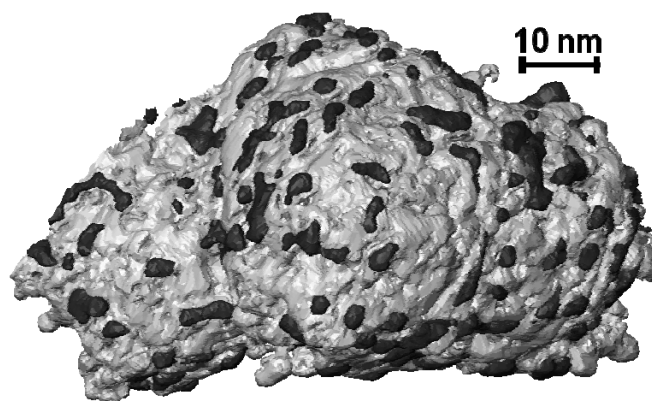


Fig. 18. Ruthenium particles (dark) on a carbon support particle (light). It is visible that the ruthenium particles are partly embedded in the carbon. With the created surface meshes it is possible to evaluate the “free” surface of the ruthenium particles that is not covered by the carbon.

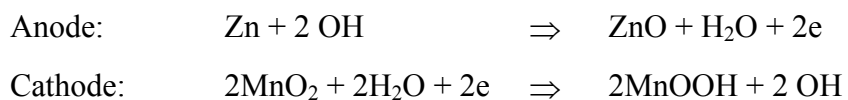
5 Batteries

The development of batteries is, alongside fuel cells, one of the most important fields in research on alternative energy supplies. Particularly in automotive applications, batteries play an important role and might become a main energy source for future short distance cars. Furthermore, batteries could complement fuel cell systems as temporary energy storage for sudden load changes, for example during acceleration of a car. In this chapter, the potential of neutron and synchrotron X-ray tomography for the investigation of structural changes during battery discharge, recharge and aging are presented.

5.1 *In-situ Characterization of batteries with synchrotron tomography*

As synchrotron and neutron tomography techniques are non-destructive and non-invasive, three-dimensional structural parameters can be mapped for a single cell without having to destroy the cell. These methods can thus produce an undistorted picture of exactly the same materials under any load cycle and over almost any length of time.

As a first example, alkaline Zn-MnO₂ batteries were investigated.^[112-116] Alkaline batteries consist of a Zn powder anode and MnO₂ at the cathode.^[117-118] During discharge, the anode zinc is oxidized and the MnO₂ is reduced by solid-state intercalation of H into the MnO₂ lattice. The main chemical processes are described by^[116-118]:



Structural changes during discharge, especially the morphology and spatial distribution of the different chemical components are of great importance.^[112,119] It is very difficult to open a cell and to investigate a section through the battery by optical or electron microscopy, or other techniques. The material is unstable in air. Oxidation and corrosion of Zn and carbonation of ZnO strongly alter the surface. In addition, the liquid electrolyte KOH requires the battery to be either frozen with liquid nitrogen or the application of special techniques to remove the electrolyte.^[112]

In contrast synchrotron X-ray tomography enables an investigation of the entire material within a battery in 3D and makes it possible to investigate pore distributions and other structural variations of the material's density with a spatial resolution down to 0.6 μm. Figure 19 shows an example of the potential of this technique obtained in a study of the discharge of

an AAA alkaline cell. The images in Fig. 19 a display exactly the same location in the cell in different stages of discharge. The zinc particles in the interior of the cell and the MnO_2 in the outer region can be clearly recognized. The zinc particles oxidize and partially dissolve in the electrolyte. This leads to a blurring of the zinc particles into a homogeneous mass (Figs. 19 a and b). The gradual dissolution of the individual zinc particles can thus be followed individually (Fig. 19 c). In addition, the 3D dataset makes it possible to find the particle size distribution and the pore size distribution, which can provide insights into the structural and morphological changes in the material during discharge (Fig. 19 d).

After 90 min of discharge some zinc particles were oxidized and partially dissolved and the local X-ray attenuation becomes weaker turning the grey scale in the images from white to bright grey. This demonstrates that ZnO can be easily separated from metallic Zn by tomography. The oxidation process begins in the outer regions of the anodic zone close to the separator and gradually moves towards the centre of the battery, while increasingly more zinc particles are oxidized. After 180 min the ZnO forms a closed ring surrounding the remaining Zn particles. At this stage, the voltage of the cell has dropped below the accepted value and can no longer be used. In contrast to previous studies this progressing oxidation effect can be observed *in-situ* at the same location in the same cell.

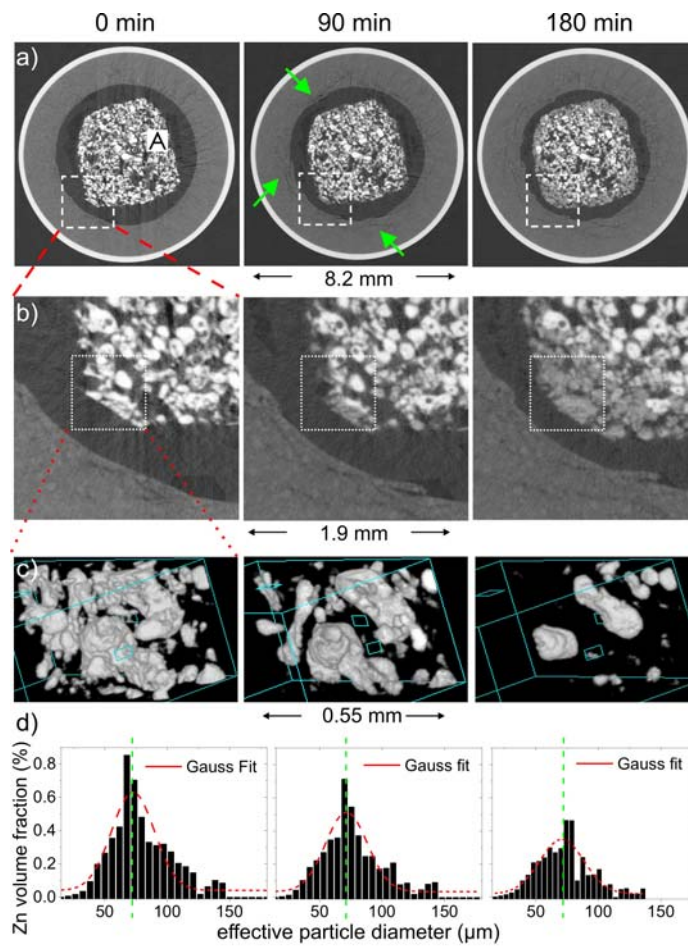


Fig. 19. Synchrotron tomography of an alkaline cell after various discharge times: 0 min., 90 min and 180 min. a) Cross section through the tomograph. The oxidation (dissolution) of the zinc powder in the electrolyte and the swelling of the MnO_2 are easy to recognize. b) Magnification of view a). c) 3D representation of the dissolving zinc particles. d) Size distribution analysis of the zinc particles. (from I. Manke et al, *Applied Physics Letters* 90, 214102 (2007). Copyright 2007, American Institute of Physics)^[119-120]

5.2 Hydrogen mapping with neutron tomography

Neutron tomography also allows for a quantification of the distribution of intercalated hydrogen. Figure 20 shows cross sections through a tomograph of a C-block cell. Due to the limited spatial resolution of $400\ \mu\text{m}$ used in this example, the metal particles and cracks in the MnO_2 are not visible here, but the hydrogen density profile can be measured. In the fully charged cell (Fig. 21, left) no significant variations in the attenuation density at the anode and cathode are visible, though the image does show variations in the electrolyte content inside the separator. The parts containing more electrolyte, possibly due to holes in the separator fleece, appear white while the regions with a very low amount of electrolyte are almost black.

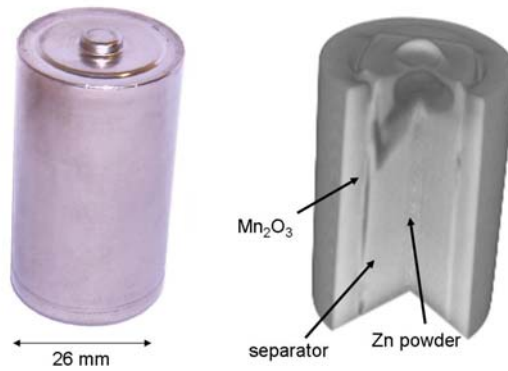


Fig. 20. Photograph of a C Block Alkaline cell (left) and a cut neutron tomograph of the cell (right).^[120]

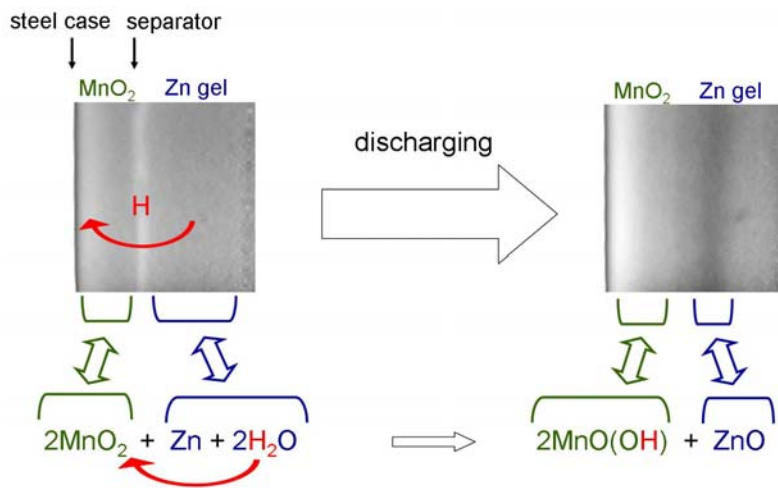


Fig. 21. Hydrogen transport during discharging of an alkaline cell. The images show cross-sections through the neutron tomogram of a fully charged (left) and almost completely discharged (right) cell.^[120]

After 24 h of discharge (Fig. 21 right image) some hydrogen at the anode is lost and has moved to the cathode. Hydrogen is shifted from the outer regions of the anode where zinc is oxidized to the outer side of the cathode close to the steel case. This results in a white and a dark stripe in the right image of Fig. 21.

5.3 Lithium batteries

Neutrons are not only sensitive to hydrogen, but also to lithium.^[1,13,121-123] Thus they are very well suited to show the 3D distribution of Li in batteries non-destructively, and to investigate discharge. The two images in Figs. 22 a and b show cross-sections through two tomographs from one LiJ battery in fully charged and partially discharged conditions (two months later) – such batteries are typically used in pacemakers.^[13,123] The structural changes in the Li

distribution can be seen clearly. When such a battery is further discharged over long periods of time (i.e. several months) the inhomogeneities in the Li distribution increase. Figure 22 c shows a 3D reconstruction of such a strongly aged and discharged LiJ battery. The deviation from the initially homogeneous distribution of the Li (white) is marked.

These examples demonstrate the possibility of illustrating changes relating to the aging and discharge conditions in Li batteries by means of neutron tomography.

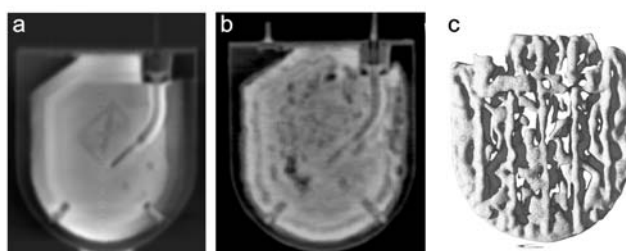


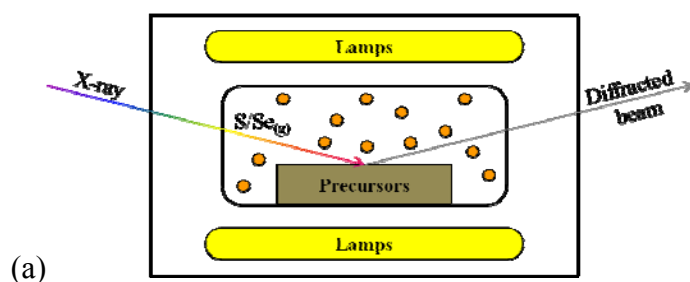
Fig. 22. Neutron tomography of a LiJ battery. a) Cross-section through the tomogram of a) a fresh cell and b) the same cell partially discharged; the Li is shown in white in each case. C) 3D representation of the Li distribution of a strongly discharged and aged battery of a similar type.^[13,123]

6 Solar cells

Chalcopyrites such as $\text{Cu}(\text{In,Ga})(\text{Se,S})_2$ (CIGS) are an attractive absorber material for thin film solar cell applications due to their band gap and high absorption coefficient.^[124-125] The complete solar cell has a structure of glass/Mo/CIGS/Buffer/ZnO. The soda-lime-glass substrate is coated by molybdenum (500 nm) as the back contact, the front contact and the window layer ZnO is separated from the CIGS absorber (1.5–2 μm) by a small buffer layer (CdS, 50 nm). The fabrication of CIGS, which is an I-III-IV₂ compound semiconductor by rapid thermal processing (RTP) was studied using energy dispersive X-ray diffraction (EDXRD) with polychromatic synchrotron radiation. The investigations were performed at the EDDI beamline at BESSY II.^[23] EDXRD allows for *in-situ* analysis of the phase formation, structural properties and elemental distribution during fast reactions.^[126] Thin film growth was investigated to determine an optimal growth path to obtain the chalcopyrite phase. The positions and the shifts of the Bragg reflections indicate the phases and residual stresses inside the layer, respectively. From the intensities of the Bragg and fluorescence signals, information on the crystal orientation and the elemental distribution can be obtained. In addition, the domain size and micro-strain can be determined by analyzing the profile shape of the Bragg reflections.

Absorber fabrication is a key process in the production of CIGS-based solar cells. Different techniques such as co-evaporation or sequential processes are applied for absorber fabrication.^[127-128] One of these sequential processes is rapid thermal processing (RTP).^[129] In this case, metallic Cu/(In,Ga) precursors are heated in a vacuum chamber under a sulfur/selenium atmosphere and chalcogenised for 3–5 min. Figure 23 a schematically illustrates the RTP chamber that was built for *in-situ* measurements at the EDDI beamline. The samples are placed inside a reactor box where heating is realized by halogen lamps above and below the samples.^[130] The temperature is measured by a thermocouple placed directly on top of a Mo-coated soda lime glass adjacent to the samples. The incoming white synchrotron beam is detected under a fixed diffraction angle of $2\theta=7.4^\circ$. The complete spectrum consisting of fluorescence and Bragg reflections, is recorded simultaneously – see Fig. 23 b – and yields the diffracted spectra before and after the RTP-sulfurization. The analysis shows that before the sulfurization process the intermetallic alloys are present while after the sulfurization reflections of CuInS₂ arise.

By taking series of spectra in time intervals of about 5 s it is possible to track the chalcopyrite synthesis *in-situ*. Figure 24 exhibits how the Bragg reflections corresponding to different phases vary with time and temperature. This allows a detailed study of the possible growth mechanisms. In this case, it was determined that the formation of CuInS₂ occurs prior to the formation of CuGaS₂.^[131] Further investigations reveal that CuInS₂ can be formed directly from the intermetallic phases, through binary sulfides or from the CuIn₅S₈-phase.^[132]



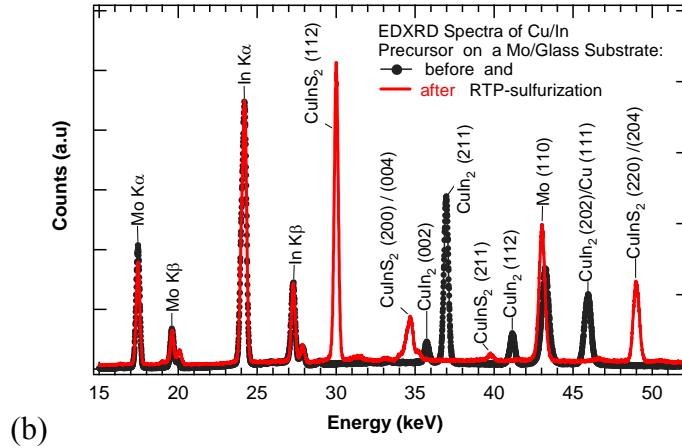


Fig. 23. (a) RTP vacuum chamber (Rapid Thermal Processing) for in-situ investigation of the growth mechanism of chalcopyrite thin films at EDDI beamline at BESSY II. (b) EDXRD (energy dispersive X-ray diffraction) spectra before (black spectrum) and after (red spectrum) the RTP-sulfurization.^[133]

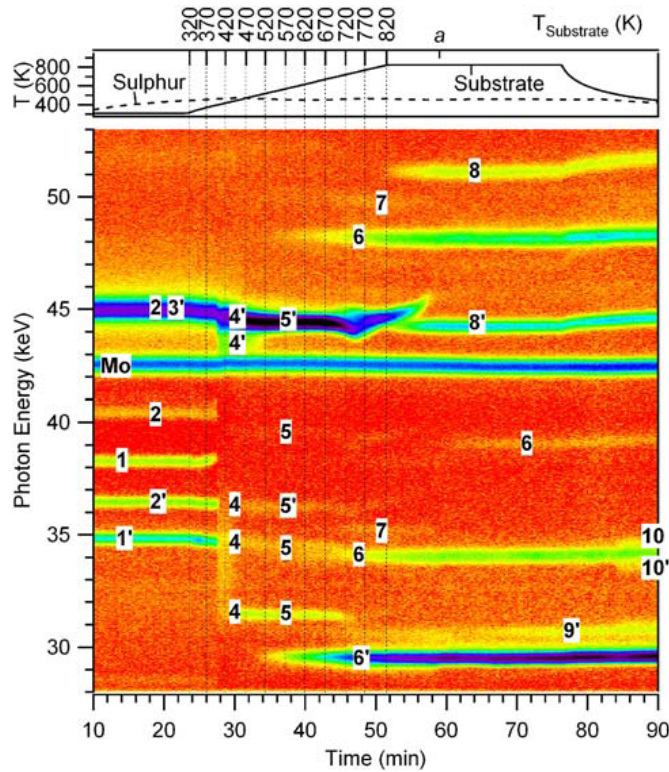


Fig. 24. In-situ EDXRD (energy dispersive X-ray diffraction) spectra acquired during the sulfurisation of a Mo/Cu:Ga/In precursor layer. Top: Temperature profile of the sample and the sulfur source of the RTP process. Bottom: Phase evolution of metallic precursors to Cu(In,Ga)S_2 . The maxima have been attributed to the phases: 1-In, 2- CuIn_2 , 3-Cu,Ga, 4- $\text{Cu}_{11}\text{In}_9$, 5- $\text{Cu}_9(\text{In,Ga})_4$, 6- CuInS_2 , 7- CuIn_5S_8 , 8-Cu,Ga, 9- CuGaS_2 , 10-CuS. The signal intensities are expressed as different colors. The measurements were done at the beamline F3 at HASYLAB (DESY).^[131]

During phase formation and growth it is of interest to track element distributions inside the layer. This can be realized by combined analyses of the Bragg and the fluorescence signals. The parameterization of the depth distribution is based on the phase information, comprised on the diffraction pattern. By comparing calculated and measured fluorescence line intensities the elemental depth distribution can be determined. This was done for the first time in a

similar setup at HASYLAB in Hamburg by Mainz *et. al.*^[134] Figure 25 a shows a modelled depth distribution at a particular time during the film growth. Figure 25 b demonstrates that after half way of the sulfurisation process the intermetallic phases are at the back contact and the chalcopyrite (CuInS_2) is at the front of the film. From these investigations it could be concluded that CuGaS_2 forms beneath a CuInS_2 layer.^[134]

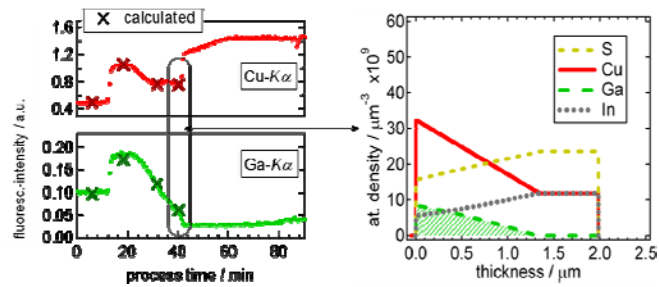


Fig. 25. (a) time developing of measures and calculated fluorescence signals during $\text{Cu(In,Ga)}_2\text{S}_2$ synthesis. (b) Modelled depth distribution at a certain point of process time.^[134]

Furthermore, the Bragg reflections provide information on the microstructure of the thin film. The Cauchy component of the integral breadth of the reflection lines can be correlated with grain size.^[135] In previous investigations it was found that for the CuInS_2 phase, the 112 reflection is suitable to analyse the microstructure evolution *in-situ*.^[136-137] In Fig. 26, the evolution of the CuInS_2 -112 reflection over time and temperature is illustrated. At moderate temperatures from 200 to 300 °C the reflections are broad and of Cauchy-type. The measured grain sizes are of the order of tens of nm (see left SEM micrograph in Fig. 26). With increasing temperature, the grains grow (right SEM micrograph) and a change of the CuInS_2 -112 reflection to a Gauss-type shape is observed. At 500 °C, the CuInS_2 film consists of grains with an average size of about 2 μm .

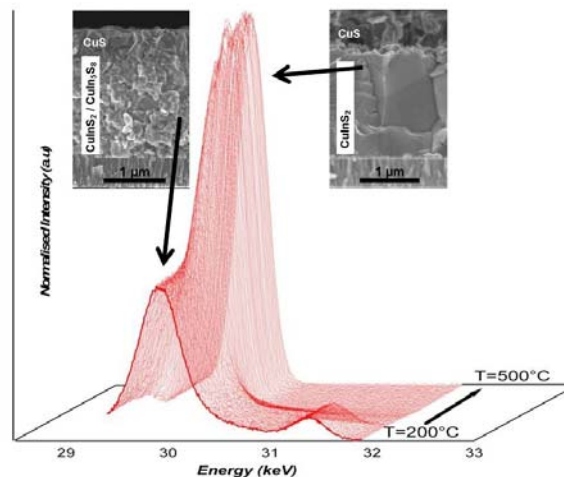


Fig. 26. CuInS₂-112 reflection as a function of temperature. At low temperature, 200-300 °C, are small grains (Cauchy-shape of the reflection) and with increasing temperatures larger grains (Gauss-shape of the reflection).^[136]

7 Summary

Synchrotron X-ray and neutron-based techniques are complementary tools for the non-destructive study of the structural and chemical properties of energy-related materials. These methods are also highly flexible and can be used for *in-situ* investigations of materials in different environments (low temperature, high temperature, vacuum, etc.). We presented a review of investigations of materials used for energy conversion and energy storage using both synchrotron X-ray and neutron and different techniques (diffraction, scattering and imaging) that were performed at the Helmholtz Centre Berlin for Energy and Materials (HZB). Several applications, including the field of fuel cells, batteries and solar cells were given and underline how useful synchrotron and neutron experiments can be. As the importance of energy research continues to grow rapidly, the study of energy-related materials will become one of the major applications for synchrotron X-ray and neutron based techniques in future.

Acknowledgements

We gratefully acknowledge the financial support of this work by the German Federal Ministry of Education and Research (BMBF) under Grant No. 03SF0324

8 References

- [1] *Advanced Tomographic Methods in Materials Research and Engineering*; J. Banhart, Ed.; Oxford University Press: Oxford, UK, 2008.
- [2] *Neutrons and Synchrotron Radiation in Engineering Materials Science*; W. Reimers, A. Pyzalla, A. Schreyer, H. Clemens, Eds.; Wiley-VCH, Weinheim 2008.
- [3] S. R. Stock. *International Materials Reviews* **2008**, *53*, 129.
- [4] M. Strobl, I. Manke, N. Kardjilov, A. Hilger, M. Dawson, J. Banhart *Journal of Physics D-Applied Physics* **2009**, *42*.
- [5] N. Kardjilov, I. Manke, M. Strobl, A. Hilger, W. Treimer, M. Meissner, T. Krist, J. Banhart *Nature Physics* **2008**, *4*, 399.
- [6] M. Dawson, I. Manke, N. Kardjilov, A. Hilger, M. Strobl, J. Banhart *New Journal of Physics* **2009**, *11*.
- [7] I. Manke, N. Kardjilov, M. Strobl, A. Hilger, J. Banhart *Journal of Applied Physics* **2008**, *104*, 076109.

- [8] M. Strobl, W. Treimer, P. Walter, S. Keil, I. Manke *Applied Physics Letters* **2007**, 91.
- [9] I. Manke, N. Kardjilov, A. Hilger, M. Strobl, M. Dawson, J. Banhart *Materials Testing-Materials and Components Technology and Application* **2008**, 50, 572.
- [10] M. Strobl, N. Kardjilov, A. Hilger, E. Jericha, G. Badurek, I. Manke *Physica B: Condensed Matter* **2009**, 404, 2611.
- [11] N. Kardjilov, I. Manke, A. Hilger, M. Dawson, J. Banhart *Advanced Materials & Processes* **2008**, 166, 43.
- [12] B. Schillinger, E. Lehmann, P. Vontobel *Physica B: Condensed Matter* **2000**, 276-278, 59.
- [13] N. Kardjilov, A. Hilger, I. Manke, M. Strobl, W. Treimer, J. Banhart *Nuclear Instruments and Methods in Physics Research Section A: Accelerators, Spectrometers, Detectors and Associated Equipment* **2005**, 542, 16.
- [14] I. Manke, M. Strobl, N. Kardjilov, A. Hilger, W. Treimer, M. Dawson, J. Banhart *Nuclear Instruments and Methods in Physics Research Section A: Accelerators, Spectrometers, Detectors and Associated Equipment* **2009**, 610, 622.
- [15] A. Hilger, N. Kardjilov, T. Kandemir, I. Manke, J. Banhart, D. Penumadu, A. Manescu, M. Strobl *Journal of Applied Physics* **2010**, 107, 036101.
- [16] M. Strobl, C. Grünzweig, A. Hilger, I. Manke, N. Kardjilov, C. David, F. Pfeiffer *Physical Review Letters* **2008**, 101, 123902.
- [17] M. Strobl, A. Hilger, N. Kardjilov, O. Ebrahimi, S. Keil, I. Manke *Nuclear Instruments and Methods in Physics Research Section A: Accelerators, Spectrometers, Detectors and Associated Equipment* **2009**, 605, 9.
- [18] W. Treimer, M. Strobl, N. Kardjilov, A. Hilger, I. Manke *Applied Physics Letters* **2006**, 89.
- [19] M. Strobl, N. Kardjilov, A. Hilger, G. Kühne, G. Frei, I. Manke *Nuclear Instruments and Methods in Physics Research Section A: Accelerators, Spectrometers, Detectors and Associated Equipment* **2009**, 604, 640.
- [20] P. Vontobel, E. H. Lehmann, R. Hassanein, G. Frei *Physica B: Condensed Matter* **2006**, 385-386, 475.
- [21] U. Matsushima, W. B. Herppich, N. Kardjilov, W. Graf, A. Hilger, I. Manke *Nuclear Instruments and Methods in Physics Research Section A: Accelerators, Spectrometers, Detectors and Associated Equipment* **2009**, 605, 146.
- [22] W. Görner, M. P. Hentschel, B. R. Müller, H. Riesemeier, M. Krumrey, G. Ulm, W. Diete, U. Klein, R. Frahm *Nuclear Instruments and Methods in Physics Research Section A: Accelerators, Spectrometers, Detectors and Associated Equipment* **2001**, 467-468, 703.
- [23] C. Genzel, I. A. Denks, J. Gibmeier, M. Klaus, G. Wagener *Nuclear Instruments and Methods in Physics Research Section A: Accelerators, Spectrometers, Detectors and Associated Equipment* **2007**, 578, 23.
- [24] G. Goerigk, H.-G. Haubold, O. Lyon, J.-P. Simon *Journal of Applied Crystallography* **2003**, 36, 425.
- [25] A. Hoell, F. Bley, A. Wiedenmann, J. P. Simon, A. Mazuelas, P. Boesecke *Scripta Mater* **2001**, 44, 2335.
- [26] A. Hoell, I. Zizak, H. Bieder, L. Mokrani *patent DE 2006 029 449* **2006**.
- [27] U. Keiderling, A. Wiedenmann *Physica B: Condensed Matter* **1995**, 213-214, 895.
- [28] C.-O. Fischer In *4t World Conference on Neutron Radiography*; J. B. Barton, Ed.; Gordon and Breach: San Francisco, USA, 1992, p 213.
- [29] N. Kardjilov, A. Hilger, I. Manke, M. Strobl, M. Dawson, J. Banhart *Nuclear Instruments and Methods in Physics Research Section A: Accelerators, Spectrometers, Detectors and Associated Equipment* **2009**, 605, 13.
- [30] H. Friedrich, P. E. de Jongh, A. J. Verkleij, K. P. de Jong *Chemical Reviews* **2009**, 109, 1613.

- [31] J. R. Kremer, D. N. Mastrorarde, J. R. McIntosh *Journal of Structural Biology* **1996**, *116*, 71.
- [32] K. J. Batenburg, S. Bals, J. Sijbers, C. Kübel, P. A. Midgley, J. C. Hernandez, U. Kaiser, E. R. Encina, E. A. Coronado, G. Van Tendeloo *Ultramicroscopy* **2009**, *109*, 730.
- [33] A. Kupsch, A. Lange, M. P. Hentschel, B. R. Müller *MP Materials Testing* **2010**, *06*, 394.
- [34] *Computed tomography reconstructions by DIRECTT-2D model calculations compared to filtered backprojection*; A. Lange, M. P. Hentschel, A. Kupsch, Eds.; Carl Hanser Verlag, 2008; Vol. 50, 272-277.
- [35] *PEM Fuel Cells: Theory and Practice*; F. Barbir, Ed.; Elsevier Academic Press San Diego, CA, 2005.
- [36] L. Carrette, K. A. Friedrich, U. Stimming *Fuel Cells* **2001**, *1*, 5.
- [37] *Fuel Cell Technology Handbook*; G. Hoogers, Ed.; CRC Press LLC: Boca Raton, FL., 2003.
- [38] *Fuel Cell Systems Explained*; 2 ed.; J. Larminie, A. Dicks, Eds.; John Wiley and Sons Ltd: Chichester 2003.
- [39] B. C. H. Steele, A. Heinzl *Nature* **2001**, *414*, 345.
- [40] C.-Y. Wang In *Handbook of Fuel Cells – Fundamentals, Technology and Applications*; W. Vielstich, A. Lamm, H. A. Gasteiger, Eds.; John Wiley & Sons: Chichester, 2003; Vol. 3, p 337.
- [41] R. C. T. Slade, J. Barker, J. H. Strange *Solid State Ionics*, *35*, 11.
- [42] T. A. Zawodzinski, C. Derouin, S. Radzinski, R. J. Sherman, T. Van Smith, T. E. Springer, S. Gottesfeld *Journal of The Electrochemical Society* **1993**, *140*, 1041.
- [43] R. Eckl, W. Zehner, C. Leu, U. Wagner *Journal of Power Sources* **2004**, *138*, 137.
- [44] M. M. Mench, Q. L. Dong, C. Y. Wang *Journal of Power Sources* **2003**, *124*, 90.
- [45] S. D. Knights, K. M. Colbow, J. St-Pierre, D. P. Wilkinson *Journal of Power Sources* **2004**, *127*, 127.
- [46] J. St-Pierre, D. P. Wilkinson, S. Knights, M. L. Bos *Journal of New Materials for Electrochemical Systems* **2000**, *3*, 99.
- [47] U. Pasaogullari, C.-Y. Wang *Journal of The Electrochemical Society* **2005**, *152*, A380.
- [48] M. Hu, A. Gu, M. Wang, X. Zhu, L. Yu *Energy Conversion and Management* **2004**, *45*, 1861.
- [49] C. Ziegler, H. M. Yu, J. O. Schumacher *Journal of The Electrochemical Society* **2005**, *152*, A1555.
- [50] C. Y. Wang, P. Cheng *International Journal of Heat and Mass Transfer* **1996**, *39*, 3607.
- [51] D. Natarajan, T. Van Nguyen *Journal of Power Sources* **2003**, *115*, 66.
- [52] F. Chen, H.-S. Chu, C.-Y. Soong, W.-M. Yan *Journal of Power Sources* **2005**, *140*, 243.
- [53] J. J. Baschuk, X. Li *Journal of Power Sources* **2000**, *86*, 181.
- [54] P. Berg, K. Promislow, J. S. Pierre, J. Stumper, B. Wetton *Journal of The Electrochemical Society* **2004**, *151*, A341.
- [55] J. H. Nam, M. Kaviany *International Journal of Heat and Mass Transfer* **2003**, *46*, 4595.
- [56] S. Litster, D. Sinton, N. Djilali *Journal of Power Sources* **2006**, *154*, 95.
- [57] C. Lim, C. Y. Wang *Electrochimica Acta* **2004**, *49*, 4149.
- [58] X. G. Yang, F. Y. Zhang, A. L. Lubawy, C. Y. Wang *Electrochemical and Solid-State Letters* **2004**, *7*, A408.
- [59] K. Tüber, D. Póczy, C. Hebling *Journal of Power Sources* **2003**, *124*, 403.
- [60] F. Y. Zhang, X. G. Yang, C. Y. Wang *Journal of The Electrochemical Society* **2006**, *153*, A225.

- [61] A. A. Kulikovskiy, T. Wuster, A. Egmen, D. Stolten *Journal of The Electrochemical Society* **2005**, *152*, A1290.
- [62] G. M. Homsy *Annual Review of Fluid Mechanics* **1987**, *19*, 271.
- [63] J. V. Maher *Physical Review Letters* **1985**, *54*, 1498.
- [64] A. Bazylak, D. Sinton, Z. S. Liu, N. Djilali *Journal of Power Sources* **2007**, *163*, 784.
- [65] G. Lin, W. He, T. V. Nguyen *Journal of The Electrochemical Society* **2004**, *151*, A1999.
- [66] R. J. Bellows, M. Y. Lin, M. Arif, A. K. Thompson, D. Jacobson *Journal of The Electrochemical Society* **1999**, *146*, 1099.
- [67] R. Satija, D. L. Jacobson, M. Arif, S. A. Werner *Journal of Power Sources* **2004**, *129*, 238.
- [68] D. S. Hussey, D. L. Jacobson, M. Arif, P. R. Huffman, R. E. Williams, J. C. Cook *Nuclear Instruments and Methods in Physics Research Section A: Accelerators, Spectrometers, Detectors and Associated Equipment* **2005**, *542*, 9.
- [69] N. Pekula, K. Heller, P. A. Chuang, A. Turhan, M. M. Mench, J. S. Brenizer, K. Ünlü *Nuclear Instruments and Methods in Physics Research Section A: Accelerators, Spectrometers, Detectors and Associated Equipment* **2005**, *542*, 134.
- [70] J. Zhang, D. Kramer, R. Shimoj, Y. Ono, E. Lehmann, A. Wokaun, K. Shinohara, G. G. Scherer *Electrochimica Acta* **2006**, *51*, 2715.
- [71] A. Turhan, K. Heller, J. S. Brenizer, M. M. Mench *Journal of Power Sources* **2006**, *160*, 1195.
- [72] J. P. Owejan, T. A. Trabold, D. L. Jacobson, D. R. Baker, D. S. Hussey, M. Arif *International Journal of Heat and Mass Transfer* **2006**, *49*, 4721.
- [73] A. B. Geiger, A. Tsukada, E. Lehmann, P. Vontobel, A. Wokaun, G. G. Scherer *Fuel Cells* **2002**, *2*, 92.
- [74] C. Hartnig, I. Manke, N. Kardjilov, A. Hilger, M. Grünerbel, J. Kaczerowski, J. Banhart, W. Lehnert *Journal of Power Sources* **2008**, *176*, 452.
- [75] I. Manke, C. Hartnig, M. Grunerbel, J. Kaczerowski, W. Lehnert, N. Kardjilov, A. Hilger, J. Banhart, W. Treimer, M. Strobl *Applied Physics Letters* **2007**, *90*, 184101.
- [76] I. Manke, C. Hartnig, N. Kardjilov, M. Messerschmidt, A. Hilger, M. Strobl, W. Lehnert, J. Banhart *Applied Physics Letters* **2008**, *92*, 244101.
- [77] M. A. Hickner, N. P. Siegel, K. S. Chen, D. S. Hussey, D. L. Jacobson, M. Arif *Journal of The Electrochemical Society* **2008**, *155*, B427.
- [78] A. Schröder, K. Wippermann, W. Lehnert, D. Stolten, T. Sanders, T. Baumhöfer, N. Kardjilov, A. Hilger, J. Banhart, I. Manke *Journal of Power Sources* **2010**, *195*, 4765.
- [79] A. Schröder, K. Wippermann, J. Mergel, W. Lehnert, D. Stolten, T. Sanders, T. Baumhöfer, D. U. Sauer, I. Manke, N. Kardjilov, A. Hilger, J. Schloesser, J. Banhart, C. Hartnig *Electrochemistry Communications* **2009**, *11*, 1606.
- [80] P. Boillat, D. Kramer, B. C. Seyfang, G. Frei, E. Lehmann, G. G. Scherer, A. Wokaun, Y. Ichikawa, Y. Tasaki, K. Shinohara *Electrochemistry Communications* **2008**, *10*, 546.
- [81] K. W. Feindel, S. H. Bergens, R. E. Wasylshen *Journal of the American Chemical Society* **2006**, *128*, 14192.
- [82] K. W. Feindel, L. P. A. LaRocque, D. Starke, S. H. Bergens, R. E. Wasylshen *Journal of the American Chemical Society* **2004**, *126*, 11436.
- [83] I. Manke, C. Hartnig, M. Grunerbel, W. Lehnert, N. Kardjilov, A. Haibel, A. Hilger, J. Banhart, H. Riesemeier *Applied Physics Letters* **2007**, *90*, 174105.
- [84] C. Hartnig, I. Manke, R. Kuhn, N. Kardjilov, J. Banhart, W. Lehnert *Applied Physics Letters* **2008**, *92*, 134106.
- [85] C. Hartnig, I. Manke, R. Kuhn, S. Kleinau, J. Goebbels, J. Banhart *Journal of Power Sources* **2009**, *188*, 468.

- [86] C. Hartnig, I. Manke, J. Schloesser, P. Krüger, R. Kuhn, H. Rieseemeier, K. Wippermann, J. Banhart *Electrochemistry Communications* **2009**, *11*, 1559.
- [87] I. Manke, C. Hartnig, N. Kardjilov, H. Rieseemeier, J. Goebbels, R. Kuhn, P. Krüger, J. Banhart *Fuel Cells* **2010**, *10*, 26.
- [88] P. K. Sinha, P. Halleck, C.-Y. Wang *Electrochemical and Solid-State Letters* **2006**, *9*, A344.
- [89] P. K. Sinha, P. P. Mukherjee, C. Y. Wang *Journal of Materials Chemistry* **2007**, *17*, 3089.
- [90] I. Manke, C. Hartnig, N. Kardjilov, A. Hilger, A. Lange, A. Kupsch, J. Banhart *Materials Testing-Materials and Components Technology and Application* **2009**, *51*, 219.
- [91] R. Eckl, R. Grinzinger, W. Lehnert *Journal of Power Sources* **2006**, *154*, 171.
- [92] C. Hartnig, I. Manke In *Encyclopedia of Electrochemical Power Sources*; x00Fc, G. rgen, Eds.; Elsevier: Amsterdam, 2009, p 738.
- [93] C. Hartnig, R. Kuhn, P. Kruger, I. Manke, N. Kardjilov, J. Goebbels, B. R. Muller, H. Rieseemeier *Materials Testing-Materials and Components Technology and Application* **2008**, *50*, 609.
- [94] R. Thiedmann, F. Fleischer, C. Hartnig, W. Lehnert, V. Schmidt *Journal of The Electrochemical Society* **2008**, *155*, B391.
- [95] R. Thiedmann, C. Hartnig, I. Manke, V. Schmidt, W. Lehnert *Journal of the Electrochemical Society* **2009**, *156*, B1339.
- [96] S. Zabler, A. Rack, I. Manke, K. Thermann, J. Tiedemann, N. Harthill, H. Rieseemeier *Journal of Structural Geology* **2008**, *30*, 876.
- [97] S. Zabler, A. Rueda, A. Rack, H. Rieseemeier, P. Zaslansky, I. Manke, F. Garcia-Moreno, J. Banhart *Acta Materialia* **2007**, *55*, 5045.
- [98] S. Fiechter, I. Dorbandt, P. Bogdanoff, G. Zehl, H. Schulenburg, H. Tributsch, M. Bron, J. Radnik, M. Fieber-Erdmann *The Journal of Physical Chemistry C* **2007**, *111*, 477.
- [99] M. A. Priestnall, V. P. Kotzeva, D. J. Fish, E. M. Nilsson *Journal of Power Sources* **2002**, *106*, 21.
- [100] D. C. Papageorgopoulos, F. Liu, O. Conrad *Electrochimica Acta* **2007**, *52*, 4982.
- [101] A. E. Comyns *Focus on Catalysts* **2007**, *2007*, 1.
- [102] S. Fiechter, P. Bogdanoff, G. Zehl, I. Dorbandt, G. Schmithals, K. Wippermann, J. Radnik, B. Richter *ECS Transactions* **2006**, *3*, 1261.
- [103] O. Solorza-Feria, K. Ellmer, M. Giersig, N. Alonso-Vante *Electrochimica Acta* **1994**, *39*, 1647.
- [104] G. Zehl, G. Schmithals, A. Hoell, S. Haas, C. Hartnig, I. Dorbandt, P. Bogdanoff, S. Fiechter *Angewandte Chemie International Edition* **2007**, *46*, 7311.
- [105] S. Haas, A. Hoell, R. Wurth, C. Rüssel, P. Boesecke, U. Vainio *Physical Review B* **2010**, *81*, 184207.
- [106] J. Haug, et al. *Nanotechnology* **2009**, *20*, 505705.
- [107] H. G. Haubold, X. H. Wang *Nuclear Instruments and Methods in Physics Research Section B: Beam Interactions with Materials and Atoms* **1995**, *97*, 50.
- [108] H.-G. Haubold, X. H. Wang, G. Goerigk, W. Schilling *Journal of Applied Crystallography* **1997**, *30*, 653.
- [109] S. Haas, A. Hoell, G. Zehl, I. Dorbandt, P. Bogdanoff, S. Fiechter *ECS Transactions* **2008**, *6*, 127.
- [110] S. Haas, G. Zehl, I. Dorbandt, I. Manke, P. Bogdanoff, S. Fiechter, A. Hoell *J. Phys. Chem. C* **2010**, submitted.
- [111] *Advances in Polymer Science*; H. B. Stuhmann, Ed., 1985; Vol. 67, 123-163.
- [112] Q. C. Horn, Y. Shao-Horn *Journal of The Electrochemical Society* **2003**, *150*, A652.
- [113] W.-B. Cai, Q. Shi, M. F. Mansuetto, D. A. Scherson *Electrochemical and Solid-State Letters* **2000**, *3*, 319.

- [114] E. J. Podlaha, H. Y. Cheh *Journal of The Electrochemical Society* **1994**, *141*, 1751.
- [115] F. Y. Cheng, J. Chen, X. L. Gou, P. W. Shen *Advanced Materials* **2005**, *17*, 2753.
- [116] L. Binder, K. Kordesch, P. Urdl *Journal of The Electrochemical Society* **1996**, *143*, 13.
- [117] *Handbook Of Batteries*; 3rd ed.; D. Linden, T. B. Reddy, Eds.; McGraw-Hill: New York,, 2002.
- [118] A. J. Bard **1985**.
- [119] A. Rack **2006**, *PhD thesis* <http://opus.kobv.de/tuberlin/volltexte/2006/1370/>.
- [120] I. Manke, J. Banhart, A. Haibel, A. Rack, S. Zabler, N. Kardjilov, A. Hilger, A. Melzer, H. Rieseemeier *Applied Physics Letters* **2007**, *90*, 214102.
- [121] D. Goers, M. Holzapfel, W. Scheifele, E. Lehmann, P. Vontobel, P. Novák *Journal of Power Sources* **2004**, *130*, 221.
- [122] M. Lanz, E. Lehmann, R. Imhof, I. Exnar, P. Novák *Journal of Power Sources* **2001**, *101*, 177.
- [123] N. Kardjilov, A. Hilger, I. Manke *Investigation of the discharge process in a LiI-battery*, BENSCH Experimental Report, 2004.
- [124] R. Klenk, J. Klaer, R. Scheer, M. C. Lux-Steiner, I. Luck, N. Meyer, U. Rühle *Thin Solid Films* **2005**, *480-481*, 509.
- [125] R. Scheer, R. Klenk, J. Klaer, I. Luck *Solar Energy* **2004**, *77*, 777.
- [126] H. Rodriguez-Alvarez, I. M. Kötschau, H. W. Schock *Journal of Crystal Growth* **2008**, *310*, 3638.
- [127] J. Klaer, et al. *Semiconductor Science and Technology* **1998**, *13*, 1456.
- [128] M. Powalla, G. Voorwinden, D. Hariskos, P. Jackson, R. Kniese *Thin Solid Films* **2009**, *517*, 2111.
- [129] K. Siemer, J. Klaer, I. Luck, J. Bruns, R. Klenk, D. Bräunig *Solar Energy Materials and Solar Cells* **2001**, *67*, 159.
- [130] H. Rodriguez-Alvarez *PhD Thesis, Technische Universität Berlin* **2010**.
- [131] R. Mainz, R. Klenk, M. C. Lux-Steiner *Thin Solid Films* **2007**, *515*, 5934.
- [132] H. Rodriguez-Alvarez, I. M. Koetschau, C. Genzel, H. W. Schock *Thin Solid Films* **2009**, *517*, 2140.
- [133] I. M. Kötschau, H. R. Alvarez, C. Streeck, A. Weber, M. Klaus, I. A. Denks, J. Gibmeier, C. Genzel, H. W. Schock *BESSY Annual Report* **2006**.
- [134] R. Mainz *PhD Thesis, Freie Universität Berlin* **2008**.
- [135] R. Delhez, T. H. d. Keijser, E. J. Mittemeijer *Fresenius Zeitschrift für Analytische Chemie* **1982**, *312*, 1.
- [136] H. Rodriguez-Alvarez, R. Mainz, B. Marsen, D. Abou-Ras, H. W. Schock *Journal of Applied Crystallography* **2010**, in press.
- [137] H. Rodriguez-Alvarez, R. Mainz, A. Weber, B. Marsen, H.-W. Schock In *Proceedings of the Materials Research Society, Spring Meeting 2009* San Francisco, U.S.A, 2009, p 1165.